

CRYSP: a Total-Body PET based on cryogenic cesium iodide crystals

S. R. Soleti[✉], P. Dietz, R. Esteve, J. García-Barrena, V. Herrero, F. Lopez, F. Monrabal[✉], L. Navarro-Cozcolluela, E. Oblak, J. Pelegrín[✉], J. Renner[✉], J. Toledo, S. Torelli[✉], and J. J. Gómez-Cadenas[✉]

Abstract—Total Body PET (TBPET) scanners have recently demonstrated the ability to significantly reduce both acquisition time and the administered radioactive dose, thanks to their increased sensitivity. However, their widespread adoption is limited by the high costs associated with the current available systems. In this context, pure cesium iodide (CsI) monolithic crystals, given their much lower cost compared with currently used rare-earth crystals, offer a promising solution to improve accessibility. When operated at cryogenic temperatures (approximately 100 K), CsI crystals exhibit one of the highest light outputs among inorganic crystals, around 10^5 photons/MeV. This results in energy resolution below 7%, millimeter-scale spatial resolution (including accurate depth-of-interaction determination), and coincidence time resolution at the nanosecond level, despite their relatively slow scintillation decay time. This study demonstrates that a TBPET scanner based on cryogenic CsI monolithic crystals might have the potential to deliver high-performance imaging at a reduced cost compared with conventional systems, paving the way for broader deployment and accessibility.

Index Terms—Biomedical imaging, Total Body PET, Positron emission tomography, Crystals, Cryogenics

I. INTRODUCTION

POSITRON emission tomography (PET) is a powerful imaging technique central to medical diagnostic applications, employing positron-emitting radionuclides to track biologically active molecules. The annihilation of the positrons produced by the radiotracer with the electrons of the surrounding environment generates back-to-back gamma rays of 511 keV, which are detected to create detailed images of functional processes within the body.

The last decade has witnessed the development of Total Body PET (TBPET) scanners with axial fields-of-view (AFOV) between 3 and 7 times that of conventional PET (CPET) apparatus. Such devices detect a large fraction of the emitted photons, thus dramatically increasing sensitivity, and allowing for simultaneous dynamic acquisition from all tissues of interest [1], [2]. TBPETs also offer the flexibility of optimizing signal-to-noise ratio (SNR), reducing the acquisition

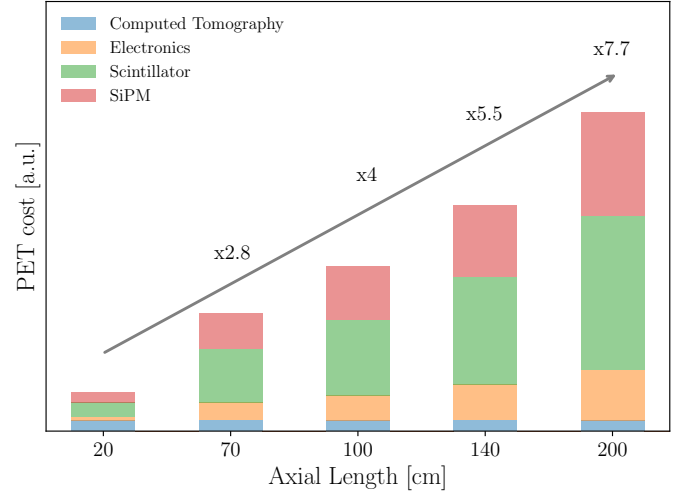


Fig. 1. Increase in component costs for a 70-cm, 100-cm, 140-cm and 200-cm system versus a system with 20 cm axial length; the y-axis is the system cost in relative units. Data taken from ref. [1].

time, or decreasing the amount of administered radioactive dose.

Prime examples of such TBPETs are the United Imaging uEXPLORER [3], and Siemens Biograph Vision Quadra [4]. The AFOV of uEXPLORER is 194 cm, while the AFOV of the smaller Quadra is 106 cm, to be compared with an AFOV of 20-30 cm typical of a CPET (e.g., the new generation General Electric Omni Legend 32 [5] has an AFOV of 32 cm). Both TBPET systems use arrays of pixelated lutetium-yttrium oxyorthosilicate (LYSO) crystals, read out by SiPMs and custom electronics, with very high sensitivity and excellent time-of-flight (TOF) resolution. The approximate increase in cost of the uEXPLORER (Quadra) compared with a typical CPET is roughly 8 (4) times (see fig. 1), well above what can be afforded by most hospitals.

The bulk of the cost in both systems comes from the scintillator, followed by the cost of the SiPMs and electronics. Of the three items, the cost of SiPMs, in large quantities, is roughly proportional to the total surface of chips deployed (not to the size of the chip), and thus proportional to the size and coverage of the scanner. However, the cost of SiPMs decreases about 5-10 % annually, with current prices about one third of those ten years ago. Thus their relative contribution to the total cost of future TBPETs will steadily decrease with time. Instead, the cost of crystals and that of the readout electronics has remained stable, and in the case of LYSO, significantly

This work did not involve human subjects or animals in its research.

S. R. Soleti (email: roberto.soleti@dipc.org), P. Dietz, F. Lopez, F. Monrabal, L. Navarro-Cozcolluela, E. Oblak, J. Pelegrín, S. Torelli, J.J. Gómez-Cadenas (email: jgomezcadenas@dipc.org) are with the Donostia International Physics Center, San Sebastián / Donostia, E-20018, Spain. L. Navarro-Cozcolluela is also with the Universidad del País Vasco (UPV/EHU), San Sebastián / Donostia, E-20018, Spain.

R. Esteve, J. García-Barrena, V. Herrero, J. Toledo are with the Instituto de Instrumentación para Imagen Molecular (I3M), Centro Mixto CSIC - Universitat Politècnica de València, Valencia, E-46022, Spain.

J. Renner is with the Instituto de Física Corpuscular (IFIC), CSIC & Universitat de València, Paterna, E-46980, Spain.

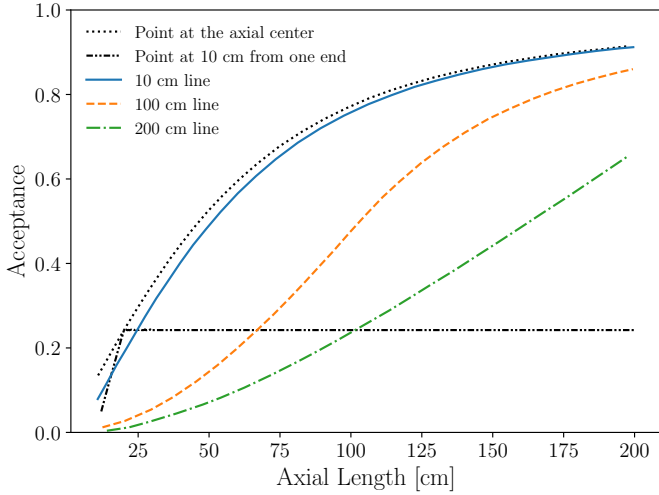


Fig. 2. The geometrical acceptance for a point-like source placed at the axial center, a point-like source placed 10 cm from one end of the scanner, and line sources of 10 cm, 100 cm and 200 cm length, as a function of the axial length. It is calculated in the transverse centre of a PET scanner with a diameter of 80 cm.

expensive. Thus, the first priority of any putative low-cost TBPET is to find significantly cheaper alternatives to LYSO. Notice that, in addition to the high cost, LYSO is a rare earth whose production and manufacturing is heavily concentrated. Last but not least, the cost of the readout electronics can be decreased for large scale production developing specific ASICs, and, importantly, reducing the number of electronics channels.

Naturally, one also desires performance comparable to that of current PET scanners. This, in turn, requires quantifying the contribution of the extended axial length of a TBPET scanner to the quality of image reconstruction.

Figure 2 shows the geometrical acceptance for two point-like sources (serving as rough approximations of small organs), one positioned at the center of a scanner with an 80 cm diameter and the other located 10 cm from one end, as a function of the axial length. For the centrally placed source, approximately 80% of the solid angle is already covered at a scanner length of 100 cm. In contrast, for the source near the edge (e.g., the brain in a TBPET), the acceptance quickly plateaus: photons emitted toward the open end of the scanner escape detection, and increasing the AFOV beyond this point offers no additional benefit. Overall, most of the gain in geometrical acceptance is achieved within the first 100 cm of axial coverage, with only marginal improvements beyond that length.

The choice for a PET scanner of 100 cm length is also motivated by the approximate axial distribution of whole-body organs of interest (e.g., brain to pelvis) for typical human height. The figure shows that, with an extended source of 100 cm, one gains in geometrical acceptance from 50% (100 cm scanner), to about 80% (200 cm scanner), a modest increased compared with cost. Thus, an AFOV of about 100 cm as implemented by the Quadra appears as a good compromise between cost and performance and a reasonable target for any TBPET proposal.

But is that extra length worth the added cost? Addressing this question requires consideration not only of the improved geometrical acceptance but also of the accompanying increase in gamma-ray absorption and Compton scattering (CS) within the patient's body, as well as the effects of parallax error (PE). These effects become more pronounced as gammas travel at increasingly oblique angles. Increased gamma absorption results in loss of events and is an unavoidable effect. CS and PE introduce an error in the reconstruction of the line-of-response (LOR), and thus contribute to image blurring. Both effects can be minimized by instrumental choices.

The impact of CS, exemplified in fig. 3, can be minimized by choosing a narrow window around 511 keV, which selects events that deposit all their energy in the crystal. The efficiency of this selection, in turn, improves with the energy resolution of the crystal. Conversely, if one selects events in a fixed energy window, the number of events which have suffered scattering in the patient's body decreases as energy resolution improves.

Conventional PET scanners are made of pixelated detectors, with crystals of small transverse dimensions and a thickness of typically 2 radiation lengths (e.g., $3.2 \times 3.2 \times 20 \text{ mm}^3$ for the Quadra). For a gamma impinging at angles normal to the crystal surface (small transaxial angles), the resolution in the transaxial coordinates depends only on the transverse size of the pixel, and the resolution on the depth of impact (d.o.i) depends on the pixel thickness. However, for large axial angles parallax error increases (see fig. 4), due to the lack of d.o.i measurement in pixelated crystals [7], [8].

Although techniques exist to compensate for CS and PE [9], their overall effect is to degrade the contribution to image reconstruction of gammas emitted at high angles and therefore to partially negate the increase in sensitivity afforded by the longer axial coverage of a TBPET.

In this paper, we propose a new type of TBPET scanner called CRYSP¹. CRYSP is based on large monolithic crystals of CsI crystals made of pure cesium iodide (CsI) operating at cryogenic temperatures. The light output of these crystals is very large (about 10^5 photons/MeV [10]–[12]), which translates into excellent energy resolution. This performance, combined with the monolithic form factor, allows to achieve a millimeter-scale spatial resolution in all three dimensions, minimizing the PE. As we will show in the next sections, these features allow to achieve performances that are comparable to the ones of current state-of-the-art TBPET scanners, at a significantly reduced cost.

This paper is organized as follows. Section II discusses the potential of pure, cryogenic CsI as scintillator material for PET, and how the choice of this material leads naturally to monolithic crystals. Section III describes the CRYSP baseline design and section IV focuses on the dedicated electronics. The modelization of the apparatus using the Geant4 simulation framework [13] is detailed in section V. Section VI discusses our strategy to reconstruct the gamma impact coordinates using convolutional neural networks (CNNs). In section VII we

¹The acronym stands simultaneously for CRYStal PET and for CRYogenic ceSium PET.

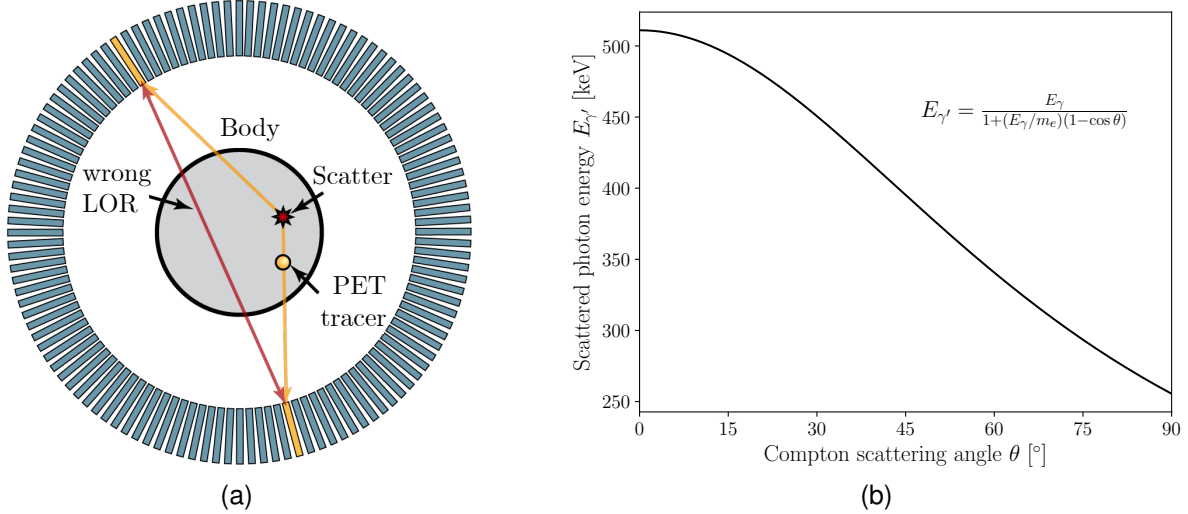


Fig. 3. (a) Compton scatter detection in PET. In Compton scattering a photon (in yellow) undergoes an interaction within the patient's body where it changes direction and loses energy. Thus, the PET scanner reconstructs a wrong LOR (in red), affecting the signal-to-background ratio of the reconstructed image. Adapted from ref. [6]. (b) The residual energy $E_{\gamma'}$ of a 511-keV incoming photon after Compton scattering with a given angle θ .

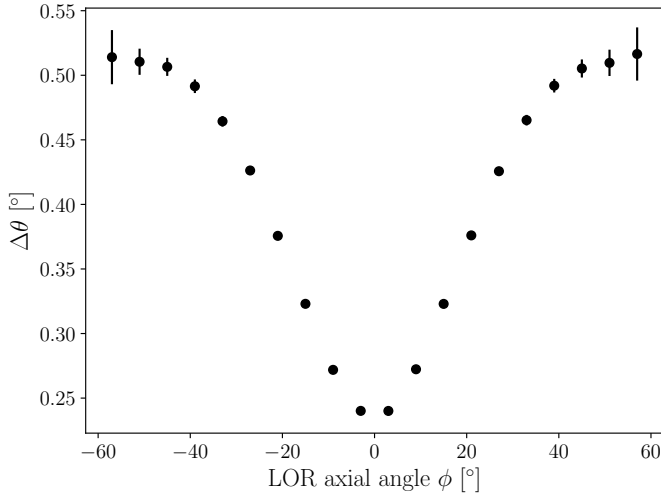


Fig. 4. Mean parallax error $\Delta\theta$, defined as the angular distance between the ideal LOR and the reconstructed LOR, as a function of the LOR axial angle. The result was obtained by simulating a PET scanner with an axial length of 1 m and a diameter of 0.8 m, made of $3 \times 3 \times 22.4$ mm³ LYSO pixels.

discuss the main parameters illustrating CRYSP performance following the NEMA guidelines (e.g., sensitivity, NECR, spatial resolution). Section VIII offers an evaluation of the apparatus performance using a modified Jaszczak phantom, comparing it with a reference detector based on pixelated LYSO crystals. Conclusions are presented in section IX.

II. CSI AS SCINTILLATOR MATERIAL FOR PET.

Table I shows the properties of cesium iodide compared with other crystals commonly used for PET. Pure CsI at ambient temperature has been adopted in particle physics for experiments set in high-rate and high-radiation environments, given its fast decay time and radiation hardness [15], [16]. However, at a first glance, its low light yield (5 photons/keV),

UV emission, average radiation length and density make it a sub-optimal candidate for PET.

Cooling pure CsI to cryogenic temperatures, approximately 100 K, causes its light emission spectrum to shift towards the near ultraviolet range, moving from around 310 nm to 340 nm [17]. This process also increases its light yield by a factor of 20, to about 100 photons/keV [10], [11], [18]. Unfortunately, its decay time also increases, approximately by a factor of 50, from 15 ns to 800 ns. In a PET scanner, the coincidence time resolution (CTR) between pairs of crystals is determined by the material's emission time profile and amount of light detected. An approximate figure of merit is given by [19]:

$$\text{CTR} \propto \sqrt{\frac{\tau}{N_{\text{p.e.}}}}, \quad (1)$$

where τ is the decay time constant and $N_{\text{p.e.}}$ is the number of detected photoelectrons.

Using eq. (1) to compare the CTR for CsI operating at ambient temperature and at 100 K we obtain:

$$\begin{aligned} \text{CTR}_{100 \text{ K}} &\approx \sqrt{\frac{800 \text{ ns}}{15 \text{ ns}} \cdot \frac{5 \text{ p.e./keV}}{100 \text{ p.e./keV}}} \cdot \text{CTR}_{300 \text{ K}} \\ &\approx 1.6 \cdot \text{CTR}_{300 \text{ K}}. \end{aligned} \quad (2)$$

Thus, since the time resolution at room temperature is at the nanosecond level [20], effective coincidence timing should be possible also at 100 K, in spite of the long decay time, as we will discuss further in section VII.

In a previous paper [12] we measured the energy resolution and coincident time resolution (CTR) for a pair of pure CsI crystals at cryogenic temperatures read out by solid state photosensors (Hamamatsu MPPCs). At $T = 104$ K, an energy resolution better than 7% FWHM and a coincidence time resolution lower than 2 ns FWHM have been achieved. While these are already very promising results, we believe

TABLE I

PROPERTIES OF SCINTILLATING MATERIALS COMMONLY USED FOR PET, COMPARED WITH SCINTILLATORS BASED ON CESIUM IODIDE. DATA FOR LYSO, BGO AND CsI(TL) HAVE BEEN OBTAINED FROM VENDOR [14]. VALUES FOR CsI WERE MEASURED IN REF. [12]. COST IS NORMALIZED BY ONE RADIATION LENGTH X_0 . THE RANGE IN PRICES DEPENDS ON THE QUALITY OF THE MATERIAL AND THE MANUFACTURING PROCESS, WITH PIXELATED BLOCKS BEING MORE EXPENSIVE THAN MONOLITHIC CRYSTALS FOR A FIXED VOLUME.

Material	Z_{eff}	X_0 (cm)	Density (g/cm ³)	Light yield (ph./MeV)	Decay time (ns)	Peak (nm)	Cost (€/cm ³ · X_0)
LYSO	66	1.14	7.4	33,000	53	420	50-80
BGO	74	1.12	7.1	9,000	300	480	25-35
CsI(TL)	54	1.86	4.5	54,000	1000	560	7-10
CsI (300 K)	54	1.86	4.5	5,000	15	310	7-10
CsI (100 K)	54	1.86	4.5	100,000	800	350	7-10

there is still room for improvement, in particular when using large monolithic crystals, SiPMs with higher PDE at 350 nm and optimized electronics. In fact, the intrinsic resolution of cryogenic CsI at 511 keV is approximately 5% [21], and one of the crystals showed a resolution of 6.3%, which we will take as default for the studies presented here. For the CTR, we use a conservative estimate of 1.5 ns, based on the 1.84 ns obtained with a tabletop setup.

III. CRYSP

The basic building block of CRYSP is a monolithic crystal, of dimensions $48 \times 48 \times 37$ mm³, where the crystal thickness corresponds to 2 radiation lengths. All crystal surfaces are polished, and five of the six faces are wrapped in PTFE to ensure a reflectivity $> 95\%$. The wrapping adds about 2 mm to the crystal transverse dimensions. Full wrapping with a good reflector is a must for energy resolution, and in the case of CsI, the relatively hard emission wavelength limits the potential reflectors, with PTFE being the best option [22]. Each crystal is read out by an array of 8×8 Hamamatsu S14160-6050HS MPPCs [23]. These photosensors have an active area of 6×6 mm² and a photon detection efficiency of approximately 38% at the emission wavelength of cryogenic CsI (see fig. 5).

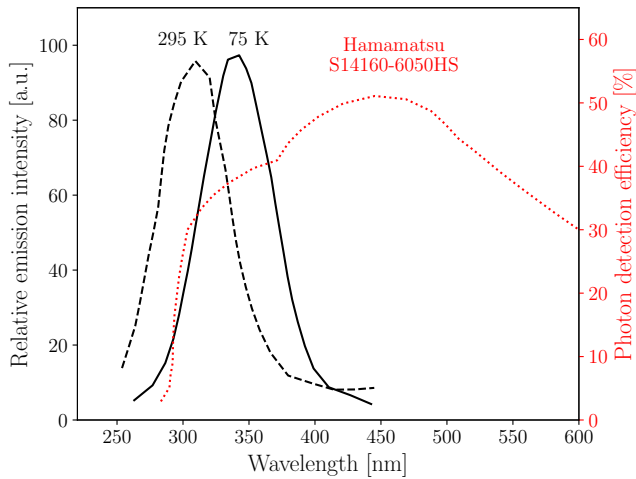


Fig. 5. CsI scintillation spectrum at room and cryogenic temperatures [17] (in black, left axis), compared with the photon detection efficiency of the Hamamatsu S14160-6050HS MPPC [23] (in red, right axis).

Thus, an interaction in the crystal results in an image of 8×8 pixels, where the intensity in each pixel is determined

by the photoelectrons recorded by each SiPM (fig. 6). System specifications are detailed in table II.

TABLE II
CRYSP1M SCANNER SPECIFICATIONS.

Parameter	Specification
Crystal size	$48 \times 48 \times 37$ mm ³
SiPM area	6×6 mm ²
SiPM model	Hamamatsu S14160-6050HS
SiPMs per crystal	64
Detector ring diameter	77.4 cm
PET AFOV	102.4 cm
Detector rings	20
Crystals per ring	48
Total number of crystals	960
Total number of channels	61,440
Energy resolution	6.3%
Energy window	465–555 keV
Coincidence time resolution	1.5 ns
Coincidence time window	4.5 ns
Operating temperature	77 K

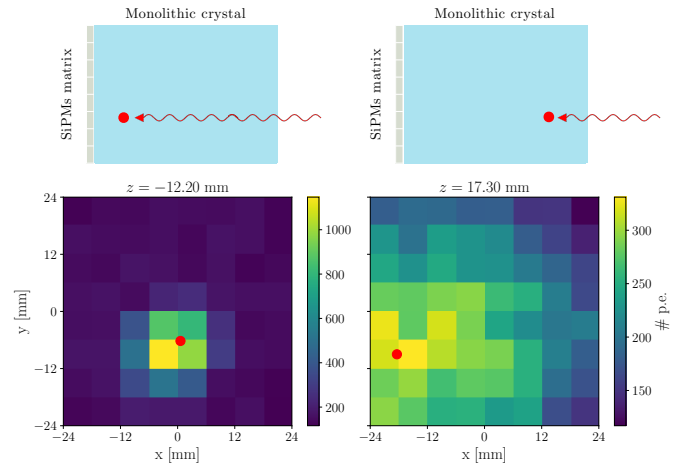


Fig. 6. Charge collected by the SiPM matrix coupled to a monolithic crystal for two different interactions, one close to the SiPMs plane ($z = -12.20$ mm) and one near the crystal entrance ($z = 17.30$ mm). The red dot corresponds to the simulated interaction point. The difference between the two patterns is exploited by a neural network to reconstruct the d.o.i. (here the z coordinate).

For definiteness, we consider a CRYSP scanner with dimensions similar to those of the Quadra (CRYSP1M). This corresponds to an effective diameter of ~ 774 mm and an effective length of ~ 1024 mm, which translates to 20 rings, where each ring is comprised of 48 crystals of $50 \times 50 \times 38$ mm³, including wrapping. Thus, CRYSP1M deploys a total of 960

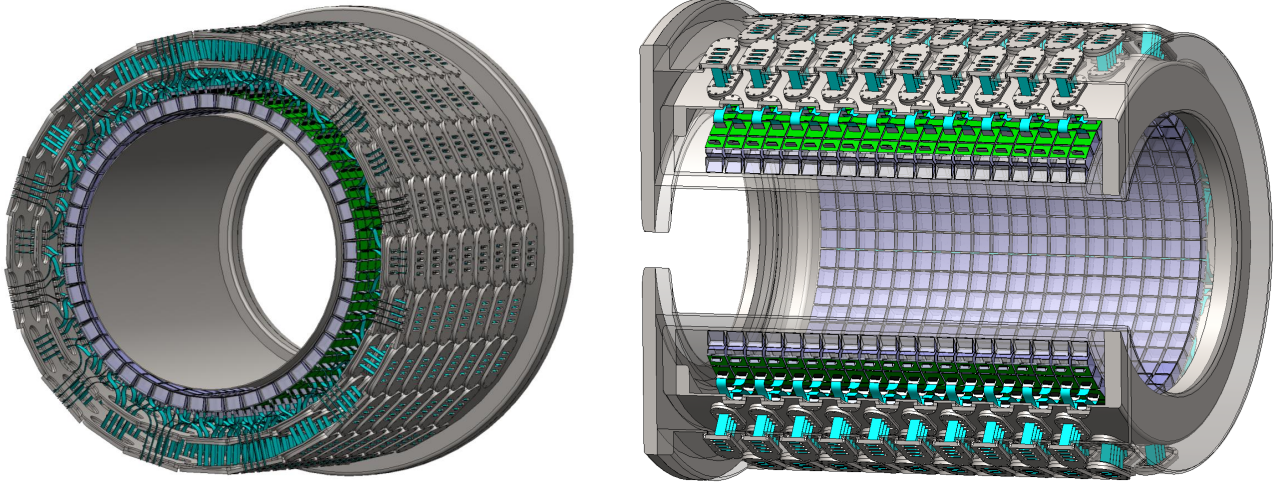


Fig. 7. CAD drawings of two sections of the CRYSP conceptual design, showing the different parts of the scanner. The crystals, in purple, are placed in a volume filled with liquid nitrogen and read out by a matrix of SiPMs, in green. This volume is separated from the environment by a thin volume at vacuum on the inner side, facing the patient, and a larger volume at vacuum on the outer side, which houses the PCB feedthroughs (in blue). These two vacuum chambers provide thermal insulation to the liquid nitrogen volume.

crystals and 61,440 channels (compared with the 243,200 of the Quadra).

Figure 7 shows a conceptual design. The scanner is hosted in a cryostat. The inner volume of the cryostat is filled with liquid nitrogen that bathes the crystals and the SiPMs, keeping them at approximately 78 K. This implies that dark current in the SiPMs is reduced, and its effect negligible, given the very high yield of the scintillator. The outer volumes of the cryostat are at vacuum and provide thermal isolation.

The total estimated heat loss of the cryostat is 20 W. Out of these losses, 70% are associated with the inner instrumentation of the SiPMs that have a direct thermal path between the inner and outer vessels. The other 30% are radiation losses assuming a 10 layer Multi-layer Insulation of aluminized Mylar surrounding the inner cryostat. The volume of liquid nitrogen evaporated per hour due to 20 W of heat loss is 0.45 L/h making a yearly consumption of 3942 L/year. The typical costs of liquid nitrogen are below 0.6 €/L in facilities with on site liquid nitrogen storage tanks, therefore the associated running costs will be close to 2,000 €/year.

Each SiPM board is connected to a simple feedthrough (e.g., a potted rigid PCB circuit, see fig. 8), that allows extracting the signal outside the cryostat, where the readout electronics are placed. The connection in between the inner and external feedthrough will be done by flexible cables allowing for the connection and mounting of the different flanges. This arrangement has already been validated in similar environments and does not represent a particular technical challenge [24].

When a gamma interacts in a crystal, the readout ASIC digitizes the charge in each of the 64 channels and sends 64×2 numbers to an FPGA, corresponding to the integrated charge and the timestamp value, as described in section IV. The FPGA computes the time of interaction assigned to the crystal (e.g., by taking an OR of the individual timestamps),

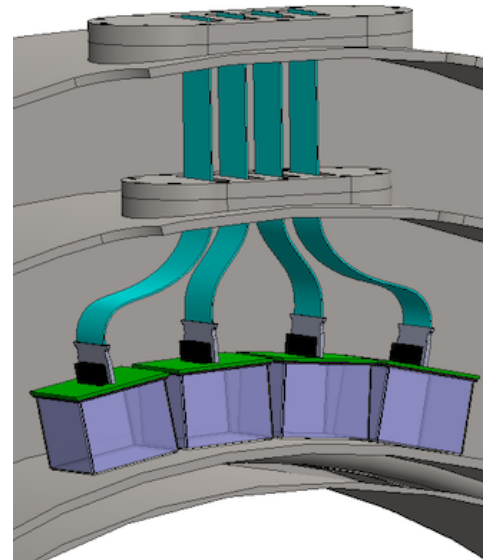


Fig. 8. Detail of the scanner showing the connection between four SiPM boards (in green), coupled to four monolithic crystals (in purple), and the exterior. In this conceptual design, the feedthroughs consist of rigid PCBs acting as feedthroughs connected to flexible cables in the vacuum region to allow for the inner connection the cables and the mounting of the flanges. A third, thinner vacuum chamber (shown at the bottom in this illustration) separates the liquid nitrogen-filled chamber from the external environment near the patient.

as well as the total energy and the interaction vertex. The latter is achieved by passing the digitized signals (the 8×8 pixels comprising the “image” provided by the crystal) in real-time through a pre-trained CNN running on the FPGA itself (see section VI). Thus, the information provided by each crystal is reduced to five numbers: time, energy and the three

coordinates of the interaction vertex.

Given the relatively long decay time of CsI ($\tau \approx 1 \mu\text{s}$), integration of the full charge requires roughly $3\tau \approx 3 \mu\text{s}$. On the other hand, the very high luminosity of the crystal results in a fast rise time, allowing for a CTR in the range of 1-2 ns, as detailed in sec. II. Consequently, the system can accommodate high event rates. While this CTR value is too large to support TOF measurements, this limitation has an upside: the requirements on the electronics, which are usually demanding in TOF-PET systems [25], [26], can be relaxed, further reducing its cost.

Although the CTR is good enough to resolve coincidences, a fraction of events will still be lost or misreconstructed because of pile-up (e.g., events in which a second gamma interacts in the crystal before the integration of the energy of the first event is over). A dedicated pile-up processor is described in section IV-B and its effect is quantified in section VII-D.

IV. ELECTRONICS FOR CRYSP

The baseline design of CRYSP1M employs front-end integration into an application-specific integrated circuit (ASIC) to bring the information processing closer to the sensors. Therefore, the functionality of the system can be enhanced introducing new features which otherwise could not be implemented offline due to the high amount of data needed to be sent to the data acquisition (DAQ) system. The proposed detector architecture enables a customization of the front-end design that exploits detected signal characteristics allowing for unique features such as event pile-up processing and optimized timestamp generation.

A. Timestamp

Any PET-oriented front-end requires a timestamp generation system with a suitable resolution in order to enable event coincidence filtering. Although CRYSP relies on energy resolution to reject Compton-scattered gammas, an enhanced coincidence filter will help to minimize accidental LORs. High-precision timestamp generating systems depend on accurate clock distribution and synchronization schemes. Moreover, this dedicated hardware must be integrated all along the DAQ data flow, even at the front-end level. This requirement implies a significant increase in costs related to electronic systems. As a consequence, a trade-off between system synchronization complexity and CTR must be observed. In order to improve the latter, a customized time-walk correction mechanism has been proposed for our integrated front-end.

The usual strategy is to approximate timestamp values by T_0 crossing time, whose precision is limited by timing resolution. A simple Time-to-Digital Converter (TDC) scheme can easily achieve resolutions below 100 ps with relatively slow clocks (20 ns period) [27] using affordable ADC converters (less than 9 bits). However, there is a significant effect related to signal slope behavior (*time walk*) that blurs effective timestamp resolution [28]. In order to reduce this effect a very low threshold can be employed. Therefore, false pulse detection probability would increase due to noise in the input stages of the front-end. Introducing control mechanisms to reject false

pulse detection would increase hardware complexity. However, a different approach will be introduced in the development of this integrated front-end: different time values of the pulse waveform will be used to predict an enhanced timestamp value.

The proposed time-walk correction algorithm relies on several threshold crossing times of the rising slope of the pulse signal (fig. 9). The time intervals between these points along with the first (and lowest) threshold crossing point T_0 , can be used to predict the true origin of the pulse signal:

$$T_S = C_0 \cdot T_0 + C_1 \cdot \Delta T_1 + C_2 \cdot \Delta T_2 + \dots + C_n \cdot \Delta T_n, \quad (3)$$

where $\Delta T_1, \Delta T_2, \dots, \Delta T_n$ correspond to the difference between consecutive threshold crossing times and T_S to the timestamp. The required weights C_0, C_1, \dots, C_n can be estimated through simulation using a simple multiple linear regression learning algorithm.

Furthermore, the final timestamp value can be computed in an analogue fashion, reducing the amount of digital data to a coarse clock period counter and the corrected TDC output value.

This mechanism is implemented on a per-channel basis, meaning the precise timestamp of the event recorded at the detector level is computed off-chip. Typically, the first timestamp among a group of channels is selected as the most accurate event timestamp.

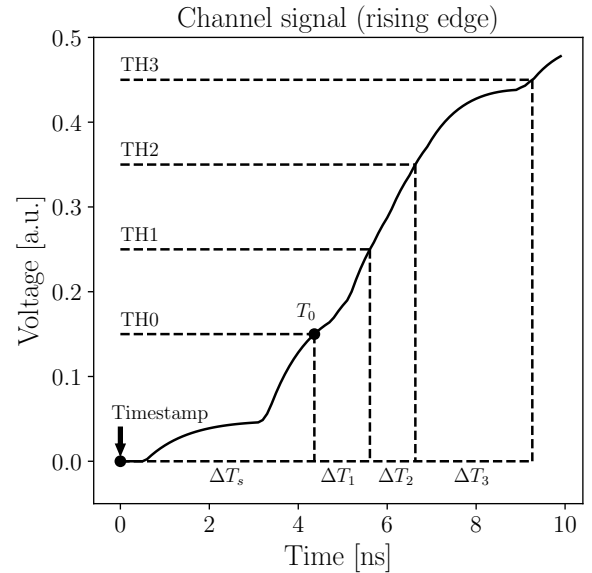


Fig. 9. The time-walk correction principle for the rising edge of a signal example. The time intervals between several threshold crossing times and the first (and lowest) threshold crossing point T_0 can be used to predict the true origin of the pulse signal.

B. Pile-up processor

Due to the long decay time of cryogenic CsI (approximately $1 \mu\text{s}$) and the use of monolithic crystals, pile-up is a significant concern in CRYSP. Thus, a novel pile-up processor based

on a peak detection mechanism [29] has been developed for the integrated front-end. For clarity, the method is illustrated using the common scenario of two overlapping pulses in a pile-up event, although it can be extended to handle multiple overlapping pulses.

The peak detection system has been enhanced to extract information from several key signal points, identified by changes in the slope sign of the input signal. To achieve this, an analog derivative computation circuit has been proposed to generate the necessary control signals. The frequency response of this circuit is critical, as it directly impacts the accuracy and limitations of the pile-up processor.

In a two-event pile-up scenario, only three key points are required to determine the energy of both events (see fig. 10). Two of these points, *A* and *C*, represent the peak positions of the first and second events, respectively. The third point, *B*, corresponds to the start of the second event, which overlaps with the tail of the first event. In an event without pile-up, the peak magnitude is directly related to the event's energy, as the signal shape consistently follows the same time distribution function. Consequently, the energy of the first event can be accurately determined from the amplitude at point *A*.

However, the energy of the second event cannot be directly inferred from the amplitude at point *C*, as the second peak is affected by the downward slope of the first event. To address this, a correction factor must be introduced to accurately determine the true peak amplitude of the second event.

This correction is based on *B* point time position related to first event starting point, and rise time value of the pulses which is a known constant value. A correction method has been proposed to obtain the right amplitude for the second pulse peak at different pile-up delays using statistical data.

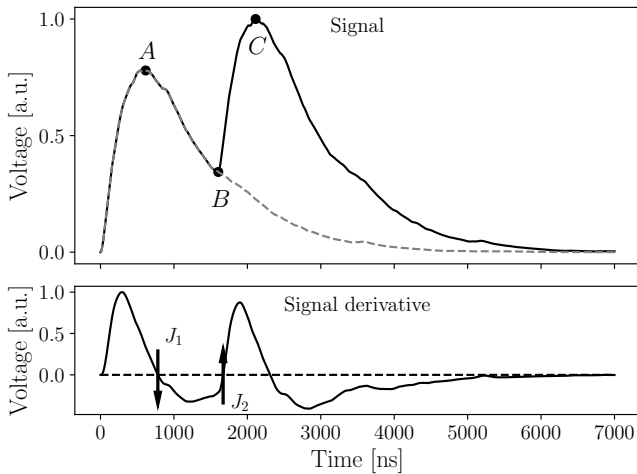


Fig. 10. Example of signal with pile-up (top) and its derivative (bottom), showing the latching times for J_1 and J_2 .

This operation is an approximation to a deconvolution of the down slope effect of the first pulse, and can be computed offline after data acquisition. Only three data must be converted to digital and sent to the DAQ system: *A* peak value, *B* time position and *C* – *B* difference (second event peak amplitude to be corrected offline). However, these data must be accurately

sampled and latched timely enough to accomplish the ADC operations. The proposed algorithm can be implemented as a modified multiple peak detector (fig. 11) whose control signals rely on the aforementioned analog derivative computation. First of all, the capacitor C_A stores the first peak and the J_1 control signal latches its value, which prevents it from losing peak information when the signal rises above it again. J_1 will be generated with the first change of the derivative signal from positive-to-negative values. At the same time, J_1 breaks C_B charge path through D_1 , so it turns into a falling peak detector along with D_2 . When J_2 is activated by a negative-to-positive change in the derivative signal, C_B gets latched with *B* point value. In the second event, C_C acts now as a peak detector along with D_1 , then the second peak value gets stored in this capacitor until the maximum value is reached.

Given the timing characteristics of the detector signals and the method used to generate the peak detector control signals, there is a limit to the allowable time overlap between pile-up pulses. A conservative estimate on this limit gives a value of approximately 500 ns. The effect of the unresolved pile-up is quantified in detail in section VII-D.

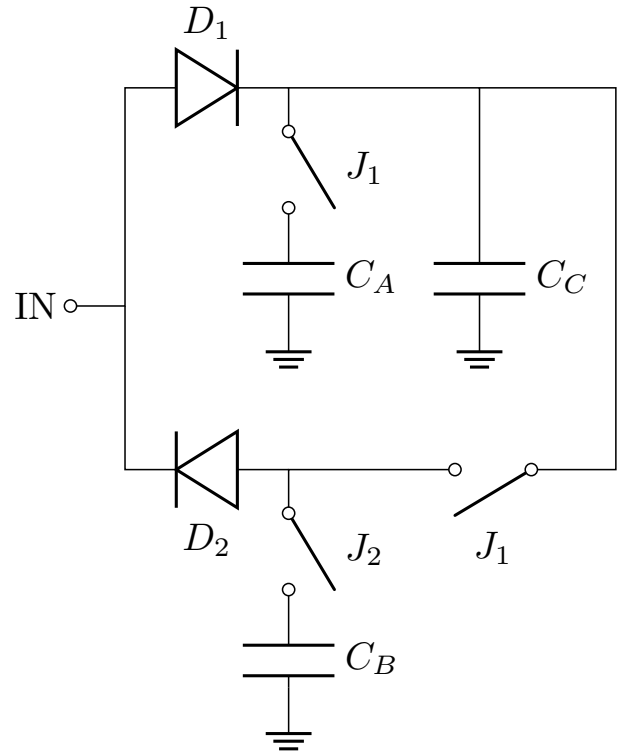


Fig. 11. Modified multiple peak detector for pile-up processing. The C_A capacitor stores the first peak, latched by J_1 upon the derivative signal's positive-to-negative transition. J_1 disables C_B charging path, turning it into a falling peak detector. J_2 , triggered by a negative-to-positive transition, latches C_B to point *B*, while C_C detects the second peak with D_1 , storing its maximum value.

V. MODELING CRYSP

A detailed microphysical simulation of CRYSP has been performed using the Geant4 simulation framework [13]. Two different applications have been implemented: one detailing a

single monolithic crystal read out by a matrix of 8×8 SiPMs of size $6 \times 6 \text{ mm}^2$ and one with the baseline design of a full CRYSP1M scanner.

The first application was used to study in detail the performances of monolithic crystals. The emission spectrum of CsI at cryogenic temperatures and the photon detection efficiency of the photosensor were specified according to fig. 5. Several possible wrapping materials (e.g., PTFE, ESR [30]) and coverage combinations were tested. The data obtained with the experimental apparatus of ref. [12] were used to validate the simulation. Optical photon generation was included in the application and the best agreement between data and Monte Carlo was obtained with the LUT optical model [31]. The results of the simulation were then used to develop the vertex reconstruction algorithm described in section VI.

The second application includes the full geometry of CRYSP1M, as shown in fig. 12, and was used for the performance evaluation detailed in sections VII and VIII. Positrons inside the phantoms were generated with a kinetic energy corresponding to the ^{18}F decay spectrum. However, simulation of optical photons is too computationally intense for a full detector. Thus, the energy deposition in the crystals is smeared with a Gaussian FWHM of 6.3%, corresponding to the experimental energy resolution obtained in ref. [12]. The light time emission profile and CTR are applied separately at analysis level.

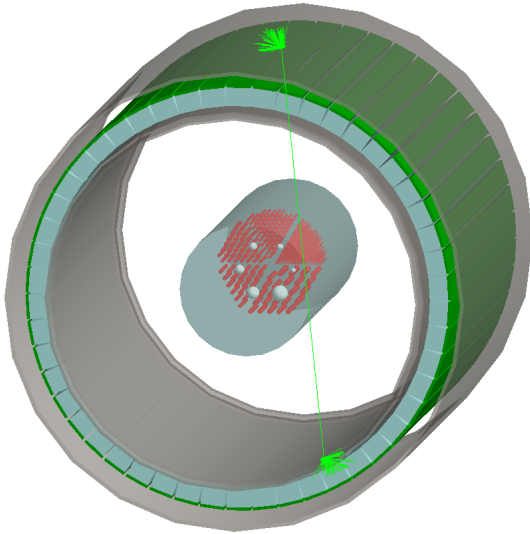


Fig. 12. Geometry simulated with Geant4 of the CRYSP1M detector with a modified Jaszczak phantom placed at the center of the FOV. An electron-positron annihilation inside the phantom produces two gamma rays which are detected by scintillating crystals. Optical photons are drawn here but not simulated in the full CRYSP1M geometry.

VI. RECONSTRUCTION OF INTERACTION VERTEX IN CRYSP

A. Convolutional neural network for vertex reconstruction

In a pixelated detector, the reconstruction of the interaction vertex (iV) usually requires a single pixel fired in the detector unit, typically built as an array of several pixels (e.g., in

the Quadra scanner, a *mini block* is made of 5×5 pixels, and each pixel has transverse dimensions of $3.2 \times 3.2 \text{ mm}^2$, thus a detector unit is a matrix of 25 pixels with dimensions $16 \times 16 \text{ mm}^2$). Imposing that the energy deposited in the pixel is near 511 keV selects events at or very near the photoelectric peak. The transverse position of the iV is known with a resolution of the order $\text{FWHM}_t = 2\sqrt{2 \ln 2} \times t / \sqrt{12}$, where t denotes the transverse dimension of the pixel. For example, in the case of the Quadra, $t = 3.2 \text{ mm}$ and thus $\text{FWHM}_t = 2.1 \text{ mm}$. The depth of interaction (d.o.i.) is known with a resolution $\text{FWHM}_{doi} = 2\sqrt{2 \ln 2} \times l / \sqrt{12}$, where l is the length of the crystal. Considering again the example of the Quadra, $l = 20 \text{ mm}$ and $\text{FWHM}_{doi} = 13.3 \text{ mm}$. Thus, while the small size of the pixels guarantees excellent transverse resolution (at the cost of a large number of channels), the d.o.i resolution is typically poor, even for dense crystals, such as LYSO or BGO, since one requires typically a minimum of 2 radiation lengths (X_0) for acceptable sensitivity. An additional problem, whose impact becomes increasingly important as the AFOV of the scanner increases, is that of parallax. Gammas entering the detectors at very large angle often do not deposit their energy in the first pixel they encounter on their trajectory, but one or two pixels further. Parallax results in large errors in the reconstruction of the iV. Additionally, gammas can scatter in one pixel, depositing a fraction of their energy, before being fully absorbed in a neighboring pixel. Such events are typically rejected, negatively impacting the sensitivity.

CsI has a longer radiation length ($X_0 \sim 18.5 \text{ mm}$) and smaller photoelectric fraction ($\sim 20\%$) than the dense, high Z_{eff} scintillators (BGO, LYSO), usually deployed in modern PET scanners. In a pixelated detector this would translate to a larger error in the d.o.i., as well as in a smaller fraction of selected events.

CRYSP, instead, proposes the use of monolithic crystals, of relatively larger dimensions, read out by an array of large-area SiPMs (see section III). One immediate advantage of such a choice is to reduce the number of readout channels by approximately a factor of 4 (from $3 \times 3 \text{ mm}^2$ to $6 \times 6 \text{ mm}^2$ SiPMs). On the other hand, the simple algorithm used for pixelated systems cannot be applied in this case, since all the 64 SiPMs reading out the crystal have signal when a gamma interacts in the crystal.

The adoption of monolithic crystals for PET and their potential regarding iV reconstruction is not a novel topic [32], [33]. However, obtaining a resolution comparable with the transverse dimensions has been historically challenging and classical algorithms fare relatively poorly [34]. Algorithms based on multilayer perceptrons have also been implemented, providing similar results [35], [36]. Here, instead, we show how excellent resolution in all three coordinates of the iV can be achieved using CNNs, which have been widely adopted for image recognition tasks with extraordinary success [37], [38].

Furthermore, the use of CNNs allows to include in the sample events with a first Compton scatter followed by photoelectric absorption, which deposit the full 511 keV in the same crystal. This is a much larger fraction than pure photoelectric events, up to 60% of the total events, and is also more significant in CsI than in higher Z_{eff} materials

such as LYSO and BGO. Most of these events deposit their energy in two or more clusters in the crystal, but the two most energetic clusters add up to a very large fraction of the total energy deposited, and thus determine the shape of the image. Notably, the first *true* interaction vertex (e.g., the point at which the gamma truly interacts in the crystal) coincides most of the time with the first *apparent* interaction vertex (e.g., the vertex closer to the entry point of the gamma), thus resulting in unbiased, gaussianly-distributed residuals between the true interaction vertex of the gamma and the first apparent vertex predicted by our CNN-based reconstruction algorithm, as shown in fig. 14.

Our CNN is, therefore, trained to search for two iVs $(x_1, y_1, z_1, x_2, y_2, z_2)$ where the index 1 is assigned to the first apparent interaction vertex. Training the CNN to find two vertices rather than one results in better determination of the position (since, in practice, an algorithm trained to find a single vertex determines the barycenter of the interaction which may be several mm away from the true vertex), and assigning the iV to the first apparent vertex is a good approximation to the true vertex. The full network is made of three consecutive convolutional blocks (Conv2D + BatchNorm + LeakyReLU + MaxPooling2D) followed by a Flatten, a Dropout, and a Dense layer yielding 6 outputs $(x_1, y_1, z_1, x_2, y_2, z_2)$, as shown in fig. 13.

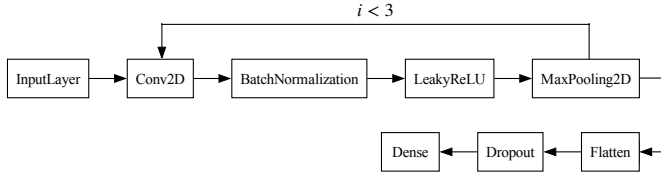


Fig. 13. Model of the neural network used to predict two iVs in the crystal, taking as input a map of the photoelectrons detected by each SiPM. The convolutional block is repeated three times and then fed to a dense layer, after passing through a flatten and a dropout layer.

The network has been trained for 10 epochs on 10^7 simulated events, with gammas uniformly distributed in the transverse plane. The result is shown in fig. 14, where the difference between the true interaction vertex and the CNN apparent vertex is plotted. The data can be well described by two Gaussians, with an effective resolution of approximately $2\sqrt{2}\ln 2 \times 1.5 \approx 3.5$ mm in all three coordinates.

The slightly larger error in the determination of the transverse coordinates, compared with pixelated PET scanners, is compensated by a much smaller error on the d.o.i. Notice, also, that the resolution in the case of a monolithic crystal stays roughly constant with the transaxial angle, since the determination of the iV is not affected by parallax (see sec. VII-B). For the spatial resolution and image reconstruction studies described in the following sections, the position of the first interaction of the gamma within the crystal is smeared with the Gaussian distributions of fig. 14.

VII. CRYSP PERFORMANCE

A. Sensitivity

The performance of CRYSP was benchmarked according to the NEMA NU 2-2018 standard [39] using a Monte Carlo simulation of the setup, produced with a dedicated Geant4 [13] application, as detailed in section V. The sensitivity of CRYSP was measured by simulating a polyethylene phantom with a length of 700 mm, an inner diameter of 2 mm, and an outer diameter of 3 mm. The positron emission was generated uniformly within the inner part of the tubing, which was filled with water. The events were selected in an energy window of 465–555 keV, which corresponds to approximately 3.5σ around the 511 keV peak, and a coincidence time window of 4.5 ns. These two selection criteria were used also for the rest of the studies of this document, as specified in table II.

According to the NEMA NU 2-2018 protocol, five different simulations were carried out, adding an aluminum sleeve with a thickness of 2.5 mm at each iteration. Finally, a sensitivity curve was plotted versus the total aluminum thickness to extract the attenuation-corrected sensitivity.

The procedure was repeated in two different configurations, one with the phantom placed at the center of the FOV and one with a radial offset of 10 cm, obtaining $R_{0\text{ cm}} = 120 \pm 5$ kcps/MBq and $R_{10\text{ cm}} = 128 \pm 5$ kcps/MBq, respectively. Although these values are lower than those reported for LYSO-based TBPETs (174 kcps/MBq for the uEXPLORER [40] and 176 kcps/MBq for the Quadra [4]), the selected events exhibit less Compton contamination due to superior energy resolution. This results in reconstructed images of comparable quality at parity of number of events (see sec. VIII).

The attenuation-corrected sensitivity as a function of the axial position for both radial offsets is reported in fig. 15.

B. Spatial resolution

Spatial resolution of the scanner has been quantified according to the NEMA standard by simulating a point-like positron source placed at six different positions: in the axial direction at the center of the AFOV and three-eighths of the AFOV from the center and in the transverse direction at 1 cm, 10 cm, and 20 cm from the center. The resolution is measured in all three directions: radially, axially, and tangentially. Table III shows the full width at half-maximum (FWHM) and full width at tenth-maximum (FWTM) amplitudes for the six positions and for maximum likelihood expectation maximization (MLEM) with 10 iterations.

C. Count rates and NECR

The count rates performance of the device is calculated by simulating a solid circular cylinder composed of polyethylene with an outside diameter of 203 mm, an overall length of 700 mm, and an internal volume of 22,000 mL. The cylinder is placed in the center of the FOV and axially aligned with the scanner. A 6.4 mm hole is added parallel to the central axis of the cylinder, at a radial distance of 4 mm, according to the NEMA specifications. Inside the hole, a tubing of length 700 mm, inside diameter of 3.2 mm, and outside diameter of

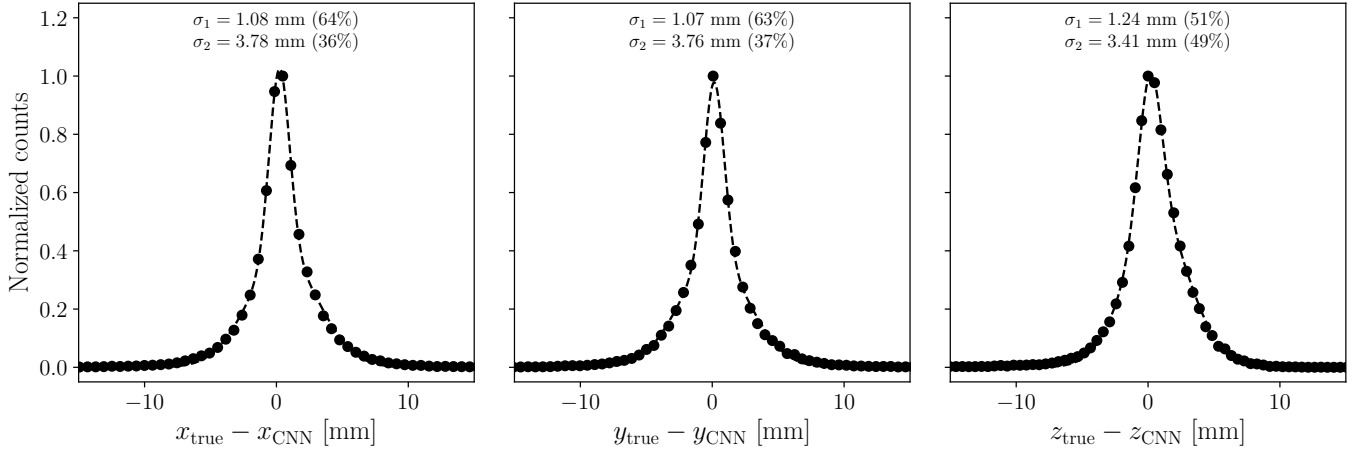


Fig. 14. Residuals between the true interaction vertex of the gamma and the first apparent vertex predicted by the CNN, in the three axes. The distributions have been fitted with the sum of two Gaussians (dashed line).

TABLE III

FWHM AND FWTM IN ALL THREE DIRECTIONS FOR POINT-LIKE SOURCES AT SIX DIFFERENT LOCATIONS, OBTAINED WITH THE MLEM ALGORITHM.

Axial position (mm)	Radial position (mm)	Full width at half-maximum (mm)			Full width at tenth maximum (mm)		
		Radial	Axial	Tangential	Radial	Axial	Tangential
512 (1/2 of FOV)	10	1.68	1.71	1.71	3.05	3.12	3.12
128 (1/8 of FOV)	10	1.68	1.71	1.71	3.06	3.11	3.11
512 (1/2 of FOV)	100	1.70	1.72	1.76	3.09	3.12	3.21
128 (1/8 of FOV)	100	1.72	1.71	1.76	3.12	3.12	3.21
512 (1/2 of FOV)	200	1.77	1.74	1.90	3.22	3.17	3.45
128 (1/8 of FOV)	200	1.85	1.80	1.99	3.36	3.28	3.62

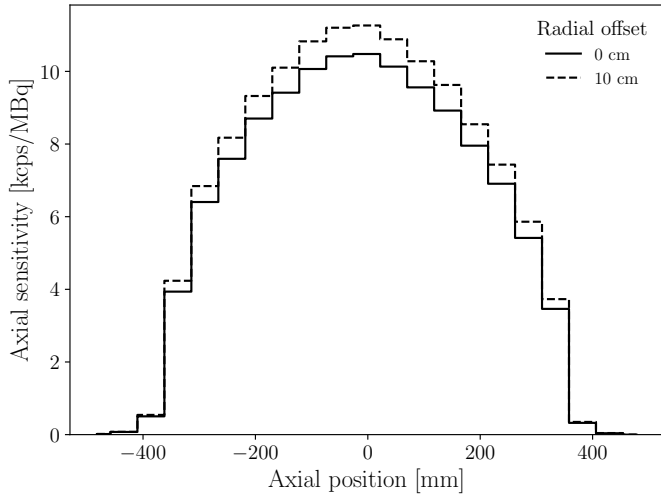


Fig. 15. Sensitivity as a function of the axial position for the CRYSP scanner with the phantom placed at the center of the FOV (solid line) and with a radial offset of 10 cm (dashed line).

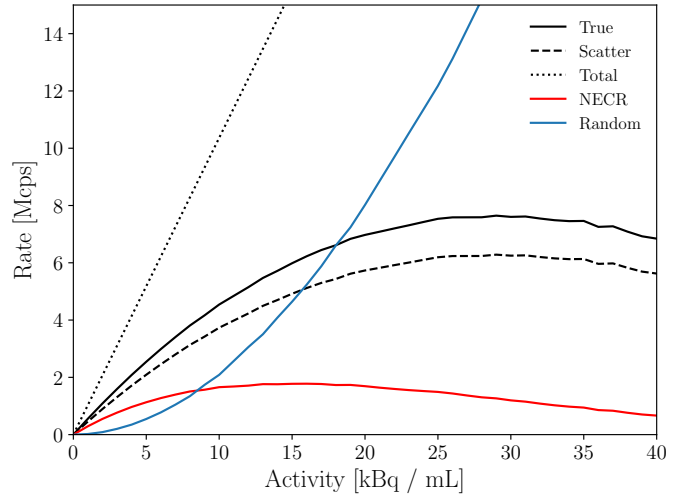


Fig. 16. True (black solid line), scatter (black dashed line), total (black dotted line), NECR (red solid line) and random (blue solid line) rates as a function of activity in the phantom tubing.

4.8 mm was inserted. In the simulation, 4.5×10^6 positrons were generated uniformly within the tubing volume. The time window was varied in order to simulate different activities, ranging from 0 to 40 kBq/mL.

Rates of total, true, scatter, and noise-equivalent counts were calculated as detailed in section 4 of the NEMA NU 2-2018 protocol and are shown in fig. 16. A peak NECR of 1.79 Mcps is obtained at an equivalent concentration of 14 kBq/mL.

D. Pile-up

In order to quantify the effect of pile-up more realistically, we simulated a simplified MIRD human phantom [41] inside CRYSP1M, using approximate relative activities in each organ as detailed in ref. [42]. Two scenarios are being considered: one where the patient's entire upper body is inside the scanner and another where the head is outside the FOV. In our simulation, signals pass through the pile-up processor described

in section IV-B. An event is classified as pile-up if the processor fails to resolve a second signal arriving within the integration window of the first. Fig. 17 illustrates the fraction of events with unresolved pile-up as a function of the activity administered to the patient. For a typical PET administered activity of 300 MBq, approximately 20% of events fall into this category. This fraction can be halved by positioning the patient's head, where a significant portion of the activity is concentrated, outside the FOV.

A key advantage of TBPETs, however, is their ability to maintain image quality with up to an order of magnitude lower administered dose, as demonstrated by uEXPLORER [43]. At an activity level of 30 MBq, this results in an almost negligible fraction of unresolved pile-up, approximately 2%.

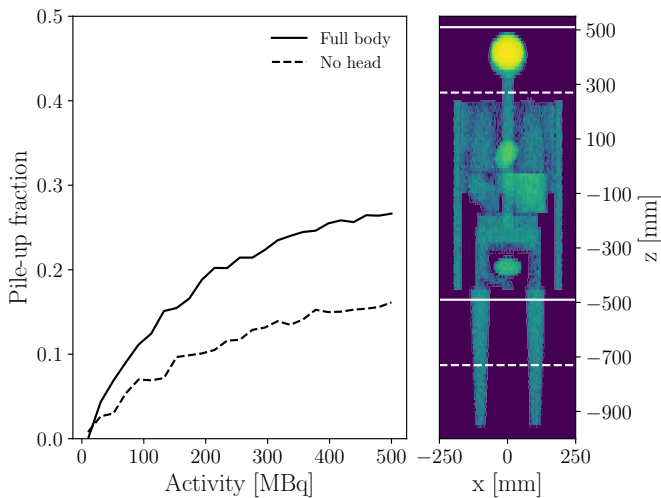


Fig. 17. Fraction of events with pile-up as a function of administered activity in two situations: one with full upper body inside the scanner (solid lines) and one with the head outside the AFOV (dashed lines). Simulation has been performed with a simplified MIRD model, shown on the right, where the color corresponds to the number of electron-positron annihilations.

VIII. IMAGE RECONSTRUCTION IN CRYSP

The quality of the images reconstructed by CRYSP represents the chief parameter to be compared with existing solutions, since it encodes sensitivity, spatial resolution, time resolution, energy resolution and NECR performances. To do so, we compare the contrast recovery coefficient (CRC) of CRYSP with the one of a simulated pixelated LYSO PET of the same size (774 mm diameter, 1024 mm length and $2 X_0$ as thickness). The pixels are assumed to have a transverse size of $3 \times 3 \text{ mm}^2$. The CTR of the simulated LYSO PET is set to 350 ps, halfway between the performances of Quadra [4] and uEXPLORER [43], which enables TOF reconstruction.

In order to better assess the impact of Compton scattering with the patient's body, we simulated a modified Jaszczak phantom with an inner diameter of 266 mm (instead of the typical 216 mm) and an axial length of 686 mm (instead of 186 mm), placed at the center of the AFOV as shown in fig. 12. Adopting a phantom with larger length and diameter allows for a more accurate estimation of Compton scattering effects in human patients. This is particularly important in a

FBPET, where a significant fraction of detected gammas is emitted at low angles and passes through substantial portions of the body, increasing the likelihood of Compton scattering. The simulation was performed with 3×10^9 electron-positron annihilation events distributed in 10 s of time, corresponding to an activity concentration of 7.9 kBq/mL. This value, although smaller than the peak NECR, has been chosen because it gives a manageable pile-up fraction of less than 20%.

The CRC was calculated for all rod radii, both for rods placed near the center of the phantom (*inner rods*) and for rods placed closer to the surface (*outer rods*), as shown in fig. 18. Reconstruction has been performed with the `parallelproj` Python package [44], which allows to run a highly-parallelized implementation of the MLEM algorithm on GPUs. The reconstruction voxel size was set to 1 mm in all three axes, a value close to the spatial resolution obtained by the CNN, and the algorithm was run for 10 iterations. Normalization and attenuation corrections were applied in both cases and no point-spread function modeling was used.

The plots show that a PET scanner based on monolithic CsI crystals has performances that can be compared with one employing LYSO pixels. Most interestingly, the CRC for rods placed near the center of the phantom is significantly better with CsI: in this case, in fact, the probability for a gamma to undergo Compton scattering in the phantom material is larger, and the extremely good energy resolution of cryogenic CsI more than compensates for the lower sensitivity and lack of TOF. For the inner rods, the CRC goes from 21% for the smallest radius (1.60 mm) to 96% for the largest one (5.55 mm). In the case of the outer rods, the variation is smaller, from 39% to 68%.

IX. SUMMARY AND FUTURE PROSPECTS

This work introduces CRYSP, a novel PET system based on cryogenic pure CsI monolithic crystals with the potential to achieve high performances at reduced costs. By operating at cryogenic temperatures, CsI offers a light yield of approximately 10^5 photons/MeV, which translates into an energy resolution below 7% FWHM. Despite its relatively slow scintillation decay time, this material can achieve a coincidence time resolution of approximately 1.5 ns, sufficient for PET applications.

Simulation studies show the ability to achieve millimeter-scale spatial resolution for interaction vertex reconstruction within a monolithic cryogenic CsI crystal. Overall, the simulated CRYSP1M scanner achieves sensitivity, NECR, and CRCs comparable to existing solutions of the same size, despite the absence of TOF capabilities. Notably, CRYSP1M performs better than a pixelated LYSO PET scanner in situations where energy resolution is critical, such as in samples with a large number of Compton-scattered gammas.

The use of cryogenics, although standard in medical diagnosis (e.g., nuclear magnetic resonance, NMR) is new in PET devices. However, and unlike NMR, CRYSP cryogenics only requires a bath of N_2 , and thus conventional, low-cost techniques for cooling and signal extraction (e.g., cheap feedthroughs) can be deployed. As a result, the cryogenics

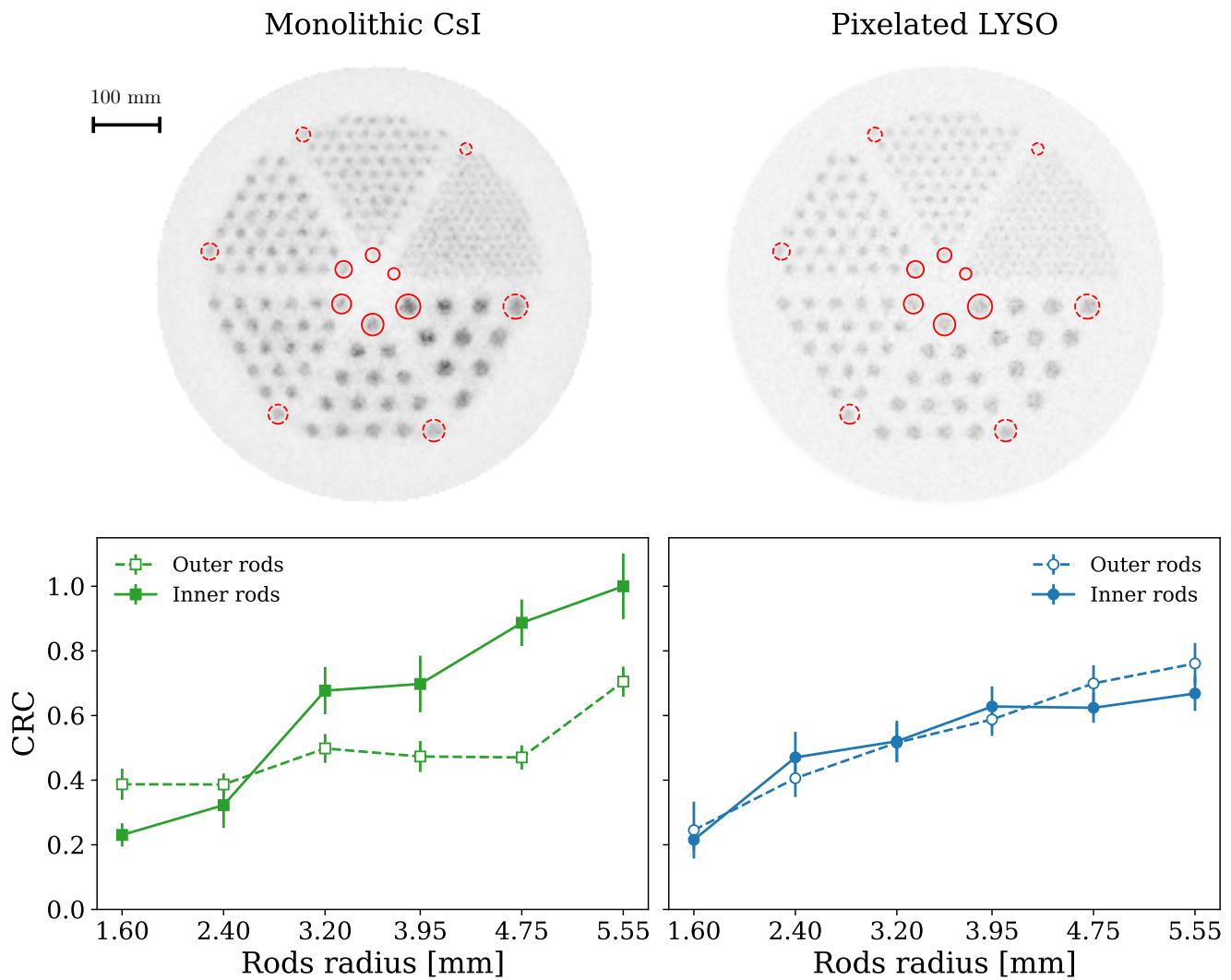


Fig. 18. Top: reconstructed images with a modified Jaszczak phantom for a PET scanner with monolithic cryogenic CsI crystals (left) and pixelated LYSO crystals (right). Normalization and attenuation corrections are applied and the color scale is the same. Bottom: contrast recovery coefficients as a function of the radius of the inner (solid) and outer (dashed) rods. The regions being considered corresponds to the red circumferences shown above.

increases the total cost of the device by less than 5% and can be implemented (again, like in the case of NMR) transparently to the final user.

In summary, CRYSP may offer a cost-effective and high-performing alternative for TBPET scanners, holding great promise for wider accessibility and utility in both clinical and research settings.

ACKNOWLEDGMENTS

The authors are thankful to Georg Schramm for the precious help with `parallelproj`.

SRS acknowledges the support of a fellowship from “la Caixa Foundation” (ID 100010434) with code LCF/BQ/PI22/11910019 and of a grant from the Basque Country Government with code PUE24-10.

JR acknowledges support from the Generalitat Valenciana of Spain under grant CIDEXG/2023/16.

REFERENCES

- [1] S. Vandenberghe, P. Moskal, and J. S. Karp, “State of the art in total body PET,” *EJNMMI physics*, vol. 7, pp. 1–33, 2020.
- [2] V. Nadig, K. Herrmann, F. M. Mottaghy, and V. Schulz, “Hybrid total-body pet scanners—current status and future perspectives,” *European journal of nuclear medicine and molecular imaging*, vol. 49, no. 2, pp. 445–459, 2022.
- [3] S. R. Cherry *et al.*, “Total-body PET: maximizing sensitivity to create new opportunities for clinical research and patient care,” *Journal of Nuclear Medicine*, vol. 59, no. 1, pp. 3–12, 2018.
- [4] G. A. Prenosil, H. Sari, M. Fürstner, A. Afshar-Oromieh, K. Shi, A. Rominger, and M. Hentschel, “Performance characteristics of the biograph vision quadra PET/CT system with a long axial field of view using the NEMA NU 2-2018 standard,” *Journal of nuclear medicine*, vol. 63, no. 3, pp. 476–484, 2022.
- [5] S. Yamagishi, K. Miwa, S. Kamitaki, K. Anraku, S. Sato, T. Yamao, H. Kubo, N. Miyaji, and K. Oguchi, “Performance Characteristics of a New-Generation Digital Bismuth Germanium Oxide PET/CT System, Omni Legend 32, According to NEMA NU 2-2018 Standards,” *Journal of Nuclear Medicine*, vol. 64, no. 12, pp. 1990–1997, 2023.
- [6] B. Weissler, “Digital PET/MRI for preclinical applications,” Ph.D. dissertation, Dissertation, RWTH Aachen, 2016, 2016.
- [7] J. P. Schmall, J. S. Karp, M. Werner, and S. Surti, “Parallax error in

- long-axial field-of-view PET scanners—a simulation study,” *Physics in Medicine & Biology*, vol. 61, no. 14, p. 5443, 2016.
- [8] S. Surti, A. R. Pantel, and J. S. Karp, “Total body PET: why, how, what for?” *IEEE transactions on radiation and plasma medical sciences*, vol. 4, no. 3, pp. 283–292, 2020.
 - [9] H. Zaidi and M.-L. Montandon, “Scatter compensation techniques in pet,” *PET clinics*, vol. 2, no. 2, pp. 219–234, 2007.
 - [10] V. Mikhailik *et al.*, “Luminescence and scintillation properties of CsI – a potential cryogenic scintillator,” *physica status solidi (b)*, vol. 252, no. 4, pp. 804–810, 2015.
 - [11] C. M. Lewis and J. I. Collar, “Response of undoped cryogenic CsI to low-energy nuclear recoils,” *Phys. Rev. C*, vol. 104, no. 1, p. 014612, 2021.
 - [12] S. R. Soleti, A. Castillo, J. I. Collar, M. del Barrio-Torregrosa, C. Echeverria, M. Seemann, D. Zerzion, and J. J. G. Cadenas, “Cryogenic cesium iodide as a potential PET material,” *JINST*, vol. 20, p. P06038, 2025.
 - [13] S. Agostinelli *et al.*, “GEANT4—a simulation toolkit,” *Nucl. Instrum. Meth. A*, vol. 506, pp. 250–303, 2003.
 - [14] Luxium, “Scintillation crystals,” <https://luxiumsolutions.com/radiation-detection-scintillators/crystal-scintillators/lyso-scintillation-crystals>, 2024.
 - [15] N. Atanov *et al.*, “Design and status of the Mu2e electromagnetic calorimeter,” *Nucl. Instrum. Meth. A*, vol. 824, pp. 695–698, 2016.
 - [16] M. Doroshenko *et al.*, “Undoped-CsI calorimeter for the K(L)0 \rightarrow π^0 ν anti- ν experiment at KEK-PS,” *Nucl. Instrum. Meth. A*, vol. 545, pp. 278–295, 2005.
 - [17] C. Amsler, D. Grögl, W. Joffrain, D. Lindelöf, M. Marchesotti, P. Niederberger, H. Pruijs, C. Regenfus, P. Riedler, and A. Rotondi, “Temperature dependence of pure CsI: scintillation light yield and decay time,” *Nuclear Instruments and Methods in Physics Research Section A: Accelerators, Spectrometers, Detectors and Associated Equipment*, vol. 480, no. 2–3, pp. 494–500, 2002.
 - [18] K. Ding, J. Liu, Y. Yang, K. Scholberg, and D. M. Markoff, “Performance of a liquid nitrogen cryostat setup for the study of nuclear recoils in undoped CsI crystals,” *Nucl. Instrum. Meth. A*, vol. 1063, p. 169283, 2024.
 - [19] M. Conti, L. Eriksson, H. Rothfuss, and C. L. Melcher, “Comparison of fast scintillators with TOF PET potential,” *IEEE Transactions on Nuclear Science*, vol. 56, no. 3, pp. 926–933, 2009.
 - [20] S. Kubota, S. Sakuragi, S. Hashimoto, and J.-z. Ruan, “A new scintillation material: Pure CsI with 10 ns decay time,” *Nuclear Instruments and Methods in Physics Research Section A: Accelerators, Spectrometers, Detectors and Associated Equipment*, vol. 268, no. 1, pp. 275–277, 1988.
 - [21] M. Moszyński, M. Balcerzyk, W. Czarnacki, M. Kapusta, W. Klamra, P. Schotanus, A. Syntfeld, M. Szawlowski, and V. Kozlov, “Energy resolution and non-proportionality of the light yield of pure CsI at liquid nitrogen temperatures,” *Nuclear Instruments and Methods in Physics Research Section A: Accelerators, Spectrometers, Detectors and Associated Equipment*, vol. 537, no. 1–2, pp. 357–362, 2005.
 - [22] M. Janecek, “Reflectivity spectra for commonly used reflectors,” *IEEE Transactions on Nuclear Science*, vol. 59, no. 3, pp. 490–497, 2012.
 - [23] Hamamatsu, “MPPC S14160-6050HS,” https://www.hamamatsu.com/eu/en/product/optical-sensors/mppc/mppc_mppc-array/S14160-6050HS.html, 2024.
 - [24] P. Ferrario, P. Collaboration *et al.*, “Status and perspectives of the PETALO project,” *Journal of Instrumentation*, vol. 17, no. 01, p. C01057, 2022.
 - [25] D. R. Schaart, “Physics and technology of time-of-flight PET detectors,” *Physics in Medicine & Biology*, vol. 66, no. 9, p. 09TR01, 2021.
 - [26] S. Pourashraf, A. Gonzalez-Montoro, M. S. Lee, J. W. Cates, J. Y. Won, J. S. Lee, and C. S. Levin, “Investigation of electronic signal processing chains for a prototype TOF-PET system With 100-ps coincidence time resolution,” *IEEE transactions on radiation and plasma medical sciences*, vol. 6, no. 6, pp. 690–696, 2021.
 - [27] J. Kalisz, “Review of methods for time interval measurements with picosecond resolution,” *Metrologia*, vol. 41, no. 1, p. 17, 2003.
 - [28] S. Xie, X. Zhang, Q. Huang, Z. Gong, J. Xu, and Q. Peng, “Methods to Compensate the Time Walk Errors in Timing Measurements for PET Detectors,” *IEEE Transactions on Radiation and Plasma Medical Sciences*, vol. 4, no. 5, pp. 555–562, 2020.
 - [29] M.-R. Mohammadian-Behbahani and S. Saramad, “A comparison study of the pile-up correction algorithms,” *Nuclear Instruments and Methods in Physics Research Section A: Accelerators, Spectrometers, Detectors and Associated Equipment*, vol. 951, p. 163013, 2020. [Online]. Available: <https://www.sciencedirect.com/science/article/pii/S0168900219313804>
 - [30] F. Loignon-Houle, C. M. Pepin, S. A. Charlebois, and R. Lecomte, “Reflectivity quenching of ESR multilayer polymer film reflector in optically bonded scintillator arrays,” *Nuclear Instruments and Methods in Physics Research Section A: Accelerators, Spectrometers, Detectors and Associated Equipment*, vol. 851, pp. 62–67, 2017.
 - [31] M. Janecek and W. W. Moses, “Simulating Scintillator Light Collection Using Measured Optical Reflectance,” *IEEE Transactions on Nuclear Science*, vol. 57, no. 3, pp. 964–970, 2010.
 - [32] A. González-Montoro, F. Sanchez, P. Bruyndonckx, G. Cañizares, J. M. Benlloch, and A. J. González, “Novel method to measure the intrinsic spatial resolution in PET detectors based on monolithic crystals,” *Nuclear Instruments and Methods in Physics Research Section A: Accelerators, Spectrometers, Detectors and Associated Equipment*, vol. 920, pp. 58–67, 2019.
 - [33] A. Gonzalez-Montoro, A. J. Gonzalez, S. Pourashraf, R. S. Miyaoka, P. Bruyndonckx, G. Chinn, L. A. Pierce, and C. S. Levin, “Evolution of PET detectors and event positioning algorithms using monolithic scintillation crystals,” *IEEE Transactions on Radiation and Plasma Medical Sciences*, vol. 5, no. 3, pp. 282–305, 2021.
 - [34] X. Li, C. Lockhart, T. K. Lewellen, and R. S. Miyaoka, “A high resolution, monolithic crystal, PET/MRI detector with DOI positioning capability,” in *2008 30th Annual International Conference of the IEEE Engineering in Medicine and Biology Society*. IEEE, 2008, pp. 2287–2290.
 - [35] M. Freire, J. Barrio, N. Cucarella, C. Valladares, A. Gonzalez-Montoro, C. de Alfonso, J. Benlloch, and A. Gonzalez, “Position estimation using neural networks in semi-monolithic PET detectors,” *Physics in Medicine & Biology*, vol. 67, no. 24, p. 245011, 2022.
 - [36] A. Iborra, A. González, A. Gonzalez-Montoro, A. Bousse, and D. Visvikis, “Ensemble of neural networks for 3D position estimation in monolithic PET detectors,” *Physics in Medicine & Biology*, vol. 64, no. 19, p. 195010, 2019.
 - [37] Z. Li, F. Liu, W. Yang, S. Peng, and J. Zhou, “A survey of convolutional neural networks: analysis, applications, and prospects,” *IEEE transactions on neural networks and learning systems*, vol. 33, no. 12, pp. 6999–7019, 2021.
 - [38] R. Yamashita, M. Nishio, R. K. G. Do, and K. Togashi, “Convolutional neural networks: an overview and application in radiology,” *Insights into imaging*, vol. 9, pp. 611–629, 2018.
 - [39] N. E. M. Association, “NEMA standards publication NU 2–2018: performance measurements of Positron Emission Tomographs,” *National Electrical Manufacturers Association*, 2018.
 - [40] B. A. Spencer, E. Berg, J. P. Schmall, N. Omidvari, E. K. Leung, Y. G. Abdelhafez, S. Tang, Z. Deng, Y. Dong, Y. Lv *et al.*, “Performance evaluation of the uEXPLORER total-body PET/CT scanner based on NEMA NU 2-2018 with additional tests to characterize PET scanners with a long axial field of view,” *Journal of Nuclear Medicine*, vol. 62, no. 6, pp. 861–870, 2021.
 - [41] A. A. Parach, H. Rajabi, and M. A. Askari, “Assessment of MIRD data for internal dosimetry using the GATE Monte Carlo code,” *Radiation and environmental biophysics*, vol. 50, pp. 441–450, 2011.
 - [42] A. H. Dias, A. K. Hansen, O. L. Munk, and L. C. Gormsen, “Normal values for 18F-FDG uptake in organs and tissues measured by dynamic whole body multiparametric FDG PET in 126 patients,” *EJNMMI Research*, vol. 12, 2022. [Online]. Available: <https://api.semanticscholar.org/CorpusID:247246383>
 - [43] R. D. Badawi *et al.*, “First human imaging studies with the EXPLORER total-body PET scanner,” *Journal of Nuclear Medicine*, vol. 60, no. 3, pp. 299–303, 2019.
 - [44] G. Schramm and K. Thielemans, “PARALLELPROJ—an open-source framework for fast calculation of projections in tomography,” *Frontiers in Nuclear Medicine*, vol. 3, p. 1324562, 2024.